Composite Structures 258 (2021) 113345

Contents lists available at ScienceDirect

Composite Structures

journal homepage: www.elsevier.com/locate/compstruct

Multi-material topology optimization of structures with discontinuities using Peridynamics

Anahita Habibian [a], Abdolrasoul Sohouli [a], Adnan Kefal [b,c,d], Ben Nadler [a], Mehmet Yildiz [b,c,d], Afzal Suleman [a,e,*]

[a] Department of Mechanical Engineering, University of Victoria, British Columbia, Canada
[b] Faculty of Engineering and Natural Sciences, Sabanci University, Tuzla 34956 Istanbul, Turkey
[c] Integrated Manufacturing Technologies Research and Application Center, Sabanci University, Tuzla 34956 Istanbul, Turkey
[d] Composite Technologies Center of Excellence, Istanbul Technology Development Zone, Sabanci University-Kordsa, Pendik 34906 Istanbul, Turkey
[e] CCTAE-LAETA, Instituto Superior Tecnico, 1049-001 Lisbon, Portugal

ARTICLE INFO

Keywords:
Topology optimization
Peridynamics
Cracked structures
Alternating active-phase algorithm
Multi-material

ABSTRACT

This study proposes an approach for solving density-based multi-material topology optimization of cracked structures using Peridynamics. The alternating active-phase algorithm is utilized to transform the multi-material problem into a series of binary phase topology optimization sub-problems. Instead of the conventional mesh-based methods, the Peridynamics theory (PD) is used as a tool to model the behaviour of the materials and solve for the displacement field. The most significant advantage of PD is its ability to model discontinuities in a relatively straightforward manner. Thus, in the present work, the effect of cracks as a discontinuity is investigated on the optimal multi-material topologies. The Solid Isotropic Material with Penalty (SIMP) method is utilized to define the material properties as a function of the design variables. Also, the optimization problem is solved through the Optimality Criteria (OC) approach. The proposed method is compared to the results reported in the literature by executing three numerical examples that investigate the effect of the direction of an interior crack on the optimal topologies. Moreover, the efficiency of the proposed approach is verified by solving several examples where we aim at minimizing the compliance of the structure with and without initial cracks.

1. Introduction

The well-known topology optimization problem (TO) has attracted attention, particularly from aerospace and automotive industries, since it was first introduced by [1]. The structural topology optimization problem deals with finding the mass/material distribution over a predefined spatial design domain by optimizing an objective function subjected to relevant constraints. Since the structures designed from an engineering perspective are usually conservative for safety reasons, they contain excessive material. To remove such excessive material, TO techniques can be readily employed. However, TO problem is inherently ill-posed, which leads to numerical instabilities, such as checkerboard patterns and mesh dependency issues. This ill-posed problem was initially solved by the introduction of the homogenization method [1], which discretizes the design domain into small elements and defines their relative densities as design variables.

Later, SIMP was introduced by [2,3]. This method originates from the homogenization approach and the design variables are the artificial relative densities of the elements. In addition, the material properties of the elements (e.g., elastic modulus) are expressed through an interpolation power function along with a penalization factor. One significant advantage of the SIMP is that it can readily be extended to include multiple materials. The SIMP method has recently become popular for topology optimization problems as a result of its conceptual simplicity, easy-to-implement nature and computational efficiency. For instance, [4] used a gradually formed continuous peak function for material interpolation and the optimality criteria (OC) to synthesize multi-material compliant structures. Their numerical examples include two/three/four-phase materials. Moreover, [5] proposed the ordered multi-material SIMP interpolation to express the material properties of the elements. Also, a combination of mass and cost constraint is considered in their work to solve the compliance minimization problem using a heuristic updating scheme of the design variables.

In 1993, Xie and Steven introduced a bio-inspired method referred to as evolutionary structural optimization (ESO) to the existing state-

* Corresponding author at: Department of Mechanical Engineering, University of Victoria, British Columbia, Canada.
E-mail address: suleman@uvic.ca (A. Suleman).

https://doi.org/10.1016/j.compstruct.2020.113345
Received 3 August 2020; Revised 8 November 2020; Accepted 13 November 2020
Available online 28 November 2020

of-the-art for TO [6]. The inspiration for the ESO method stems from the evolution of naturally occurring structures such as bones and trees.During optimization, the ESO algorithm removes the excessive material iteratively until a set of predefined volume constraints are satisfied. Later,bi-directional ESO (BESO) was proposed by [7] to search for all possible directions, including not only material removal but the addition of material to elements with high-stress levels. Many works have been dedicated to the BESO method over the last two decades and solved various complex topology optimization problems.

Another common approach in topology optimization is the Level-set method [8,9], which monitors the geometry changes of the boundaries by the motion of level sets. One notable drawback of this approach is its slow convergence rate. Also, its final solution significantly depends on the initial design, thereby posing another shortcoming. Up to date, the level-set method has been utilized for various single material topology optimizations. For example, optimal geometry of functionally graded structures were determined using this approach [10]. Another application of the level-set method involves multi-material topology optimization problems. Specifically, [11] generalized the level-set based approach using a multi-phase model proposed in [12] to solve the stress-related multi-material topology optimization. Later, [13] proposed a new Multi-Material Level Set (MM-LS) topology description for shape optimization of multi-material structures.

Recently, the alternating active-phase algorithm is introduced by [14] to extend the topology optimization solvers from the traditional binary phase to multi-phase. In this approach, a multi-phase TO problem is sequentially split into a series of binary phase sub-problems. The benefits of the alternating active-phase algorithm are its simplicity, generality, and ease of implementation. However, it has some shortcomings such as its limited application due to the fact that it is a monotonic optimization solver and thus it cannot be used for non-monotonic problems. Later, [15] used this algorithm to design three-phase compliant mechanisms, including a gripper, an inventor, and a cruncher. To validate the results, the maximum displacement of the compliant mechanisms is compared with the results obtained from a finite element based software.

Most of the works mentioned above employed mesh-dependent methods. However, some issues limit the use of mesh-based numerical methods for topology optimization applications. For instance, when dealing with large deformation or moving boundaries, re-meshing the finite element model is inevitable. Furthermore, introducing failure (e.g., cracks) to the structure is a mathematically complex procedure. To overcome these difficulties, topology optimization based on meshless methods has emerged. The most common meshless methods in TO are as follows: smooth particle hydrodynamics (SPH) [16], element-free Galerkin (EFG) [17], meshless local Petrov–Galerkin (MLPG) [18], and reproducing Kernel particle method (RKPM) [19]. Recently, meshless methods have achieved significant progress. For example, [20] used the global weak form of the EFG method with compactly supported radial basis functions (CSRBFs) as an interpolation method to construct the shape functions. Also, [21] applied the EFG method to analyze multi-material structures. A combination of Shepard interpolation and Moving Least Square (MLS) is chosen to build the shape functions. Moreover, [22] coupled FEM and EFG method to reduce the computational cost. This method can guarantee the continuity of the shape function in the coupling areas.

The presence of discontinuities, such as cracks, and hidden failures is a prevalent issue for most of the engineering structures. When the crack is not considered in the analysis, despite its existence, the optimal design cannot be reliable. Therefore, using topology optimization plays a vital role to achieve reinforced structures that can endure even with embedded cracks. However, up to date, only a few works are dedicated to this matter. To give an instance, [23] used the EFG method along with BESO to find the optimal design of a single-material structure with initially embedded cracks. They studied the effect of crack size and location on the final topology as well. Later, the idea of topology optimization of cracked structures was extended to multi-material cases. In this regard, [24] introduced a novel mesh-based numerical approach using the alternative active-phase algorithm. Moreover, they investigated the dependence of the designs on the size, location, orientation, and the number of initial cracks.

In addition to the particle-based methods mentioned above, Peridynamics (PD) [25–27] is another meshless approach; a nonlocal theory, that belongs to the class of continuum mechanics formulations. In Classical Continuum Mechanics (CCM), the governing equation of a continuum body is a partial differential equation containing spatial derivatives. Although when discontinuities such as cracks exist in the body, these well established equations face difficulties as a result of singular spatial derivatives. To tackle this problem, some approaches have been proposed, such as Linear Elastic Fracture Mechanics (LEFM) and Cohesive Zone Model (CZM). In PD, a body is subdivided into material points taking volume in space. Unlike CCM formulation, PD uses integrodifferential equations instead of partial differential equations which do not contain any spatial derivatives. Consequently, PD is an attractive candidate for modelling problems including discontinuities, and the material does not necessarily require to remain continuous after deformation.

One of the most significant benefits of PD is its ability to predict damage with no need for an external damage law for crack initiation and propagation. Additionally, damage can naturally nucleate in an unspecified location and cracks can grow through unguided paths without any singularity. Furthermore, multiple damage sites and their complex interactions can emerge in the same area. Therefore, the PD method has been successfully used to simulate crack growth [27] and failure on multi-scale structures [28], as well as damage prediction of different materials, such as composites [29,30] and layered heterogeneous materials [31]. PD also has proven to be a powerful tool to capture different types of fractures. For instance, [32] used PD to study dynamic fracture. Further studies were done to analyze the dynamic fracture of various types of structures, including concrete structures [33], anisotropic [34] and functionally graded materials [35,36]. Moreover, it is shown that Peridynamic theory can be utilized to study fatigue. E.g., [37] proposed a fatigue model to predict damage in laminates under cyclic loading.

Considering PD's ability to permit and predict discontinuities, PD-based topology optimization can provide a powerful platform to account for such imperfections so that structures can be improved at the conceptual design phase. The first attempt to merge PD with TO for cracked structures was made in [38], where the authors utilized the direct solution approach to solve PD equations at each optimization step. This innovative coupling was named as PD-TO, which yields in computationally efficient analysis for topology optimization of structures with initially embedded cracks. The PD-TO was first established based on the BESO approach. Recently, it was successfully extended to gradient-based topology optimization algorithms and extensively validated for complex engineering problems involving cracks [39].

To the best of authors' knowledge, none of the above-mentioned works used PD-TO method to analyze multi-material structures with initially embedded cracks. The only study that investigated toplogy optimization of cracked multi-material structures is [24], which uses the X-FEM method. However, one of the drawbacks of X-FEM is its requirement for external criteria, such as virtual crack closure or maximum stress techniques to introduce cracks. Also, it needs other methods, e.g. level-set, to track crack propagation. In case of complex crack paths, where a crack is embedded in the element boundaries without cutting the edges, or in case of the presence of more than one crack in an element, the X-FEM approach poses various challenges when following complex crack paths. On the other hand, the nature of PD theory enables us to define cracks or defects within the structure in a straightforward manner, and no complicated mathematical expression

is required to predict crack initiation, growth pattern and fracture modes. Moreover, PD theory can easily handle problems with moving boundaries and large deformations since there is no need to maintain mesh connectivity. As a result, using PD theory can be more beneficial for topology optimization of cracked structures as compared to X-FEM. Hence, the main novelty of this study is to introduce multi-material topology optimization of cracked structures based on PD-TO for the first time in the literature. It should be noted that multi-material designs are a class of composite structures.

It is worth mentioning that the focus of the current work is on multi-material topology optimization problems with volume constraints. However, there are some ongoing researches in multi-material topology optimization to impose the total mass constraint instead of the total volume constraint [40,41,5,42]. This problem would be an interesting topic for the future work in multi-material topology optimization utilizing the OC approach.

This paper is organized as follows. Section 2 briefly reviews the Peridynamics theory and the direct method for solving the PD equations. Section 3 introduces the minimization of compliance problem through the alternating active-phase algorithm. Next, the optimality criteria method is explained in Section 4, followed by the description of filtering concept in Section 5. Investigation and examples for the proposed multi-material PD-TO approach are discussed in Section 6. Finally, conclusions are provided in Section 7.

2. Peridynamics

To obtain the response of a solid structure subjected to external forces, the classical continuum mechanics assumes the structure as a continuous body, by ignoring its atomic structure. In continuum mechanics, the body consists of an infinite number of infinitesimal volumes called material points. These material points interact only with other ones located in their immediate vicinity. Conversely, in PD, the behavior of a material point is governed by its interactions with all material points within its range. The range of particle $\boldsymbol{x}$ is denoted by $\delta > 0$, referred to as the horizon. Also, the material points within the distance δ of $\boldsymbol{x}$ are called the family of $\boldsymbol{x}, H$, as illustrated in Fig. 1.

There are two main groups of peridynamic formulation as bond-based and state-based PD. The former formulation accounts for the interaction of material point $\boldsymbol{x}$ and its family members $\boldsymbol{x}'$ in a pairwise manner. The resulting force vectors $\boldsymbol{f}$ and $\boldsymbol{f}'$ acting at material points $\boldsymbol{x}$ and $\boldsymbol{x}'$, respectively are in opposite directions with equal magnitude. This force depends on the stretch between these material points. However, in state-based PD, the interaction force vectors can have different directions and magnitudes, since these forces rely on the deformation state of all family members of $\boldsymbol{x}$ and $\boldsymbol{x}'$. In this study, the bond-based PD is adopted due to its simplicity for coding implementation.

According to [25], the equation of motion applicable whether or not there exists discontinuities in the body can be expressed as:

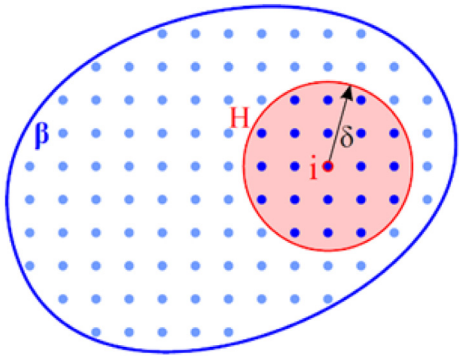

Fig. 1. family of the material point i [38].

$$\rho(\boldsymbol{x})\ddot{\boldsymbol{u}}(\boldsymbol{x},t) = \int_H \boldsymbol{f}(\boldsymbol{x}'-\boldsymbol{x},\boldsymbol{u}'-\boldsymbol{u},t)dH + \boldsymbol{b}(\boldsymbol{x},t) \tag{1}$$

In (1), the domain of integration, H, includes all the material points that interact with material point $\boldsymbol{x}$ and can be defined as:

$$H = \{\boldsymbol{x} \in \beta : ||\boldsymbol{x}'-\boldsymbol{x}|| \leqslant \delta\} \tag{2}$$

Also, $\rho(\boldsymbol{x}), \boldsymbol{b}(\boldsymbol{x},t)$, and $\ddot{\boldsymbol{u}}(\boldsymbol{x},t)$ represent the mass density, body force, and acceleration of the material point $\boldsymbol{x}$, respectively. The pairwise interaction force density between material points $\boldsymbol{x}$ and $\boldsymbol{x}'$ is denoted by $\boldsymbol{f}(\boldsymbol{x}'-\boldsymbol{x},\boldsymbol{u}'-\boldsymbol{u},t)$. This force density is a function of the relative position vector, $\boldsymbol{x}'-\boldsymbol{x}$, and relative displacement vector, $\boldsymbol{u}'-\boldsymbol{u}$. To satisfy the angular momentum balance law, in bond-based PD, it is assumed that the interaction force is along the same direction as the relative position of the two material points in the deformed configuration, $\boldsymbol{y}'-\boldsymbol{y} = (\boldsymbol{x}'+\boldsymbol{u}')-(\boldsymbol{x}+\boldsymbol{u})$, and is linearly dependent on the stretch between the two material points. The stretch of a PD bond is defined as:

$$s = \frac{|\boldsymbol{y}'-\boldsymbol{y}| - |\boldsymbol{x}'-\boldsymbol{x}|}{|\boldsymbol{x}'-\boldsymbol{x}|} \tag{3}$$

Hence, for an elastic isotropic material, the PD force can be expressed as:

$$\boldsymbol{f} = cs\frac{\boldsymbol{y}'-\boldsymbol{y}}{|\boldsymbol{y}'-\boldsymbol{y}|} \tag{4}$$

The material parameter, c, also known as bond constant, can be related to the engineering material constants through equating the strain energy densities of the PD and CCM theories for a material point due to simple loadings, including isotropic expansion and simple shear. For a linear isotropic material in 2-D analysis, the bond constant reads:

$$c = \frac{9E}{\pi h\delta^3} \tag{5}$$

where E is the elastic modulus, and h represents the thickness of a 2-D domain. Note that, in the case of bond-based PD, the strain energy equilibrium between CCM and PD results in the Poisson's ratio, ν of $1/3$.

The total strain energy of the body, U, can be calculated as:

$$U = \int_\beta W(\boldsymbol{x},t)d\beta = \frac{1}{4}\int_\beta \int_H cs^2|\boldsymbol{x}'-\boldsymbol{x}|dHd\beta \tag{6}$$

where $W(\boldsymbol{x},t)$ is the strain energy density of a material point $\boldsymbol{x}$.

The PD equation of motion in (1), is an integro-differential equation. Therefore, the solution to this equation can be conducted through numerical techniques for spatial and time integration. The spatial integration can be performed by utilizing a meshless method due to its simplicity. Additionally, it serves as a useful discretization strategy for modelling discontinuities such as cracks, voids, etc. Hence, the domain can be divided into a finite number of subdomains (e.g., quadrilateral for 2-D regions). After discretization, the material points associated with specific volumes are placed in the subdomains. Consequently, the volume integration in (1) can be approximated as:

$$\rho(\boldsymbol{x}_i)\ddot{\boldsymbol{u}}(\boldsymbol{x}_i,t) = \sum_{j=1}^{N_f}\boldsymbol{f}\left(\boldsymbol{x}_j-\boldsymbol{x}_i,\boldsymbol{u}\left(\boldsymbol{x}_j,t\right)-\boldsymbol{u}(\boldsymbol{x}_i,t)\right)V_j + \boldsymbol{b}(\boldsymbol{x}_i,t) \tag{7}$$

where $\boldsymbol{x}_i$ and $\boldsymbol{x}_j$ are the position vectors located at the ith and jth material points, respectively. N_f is the number of family members of particle i. j is a material point inside the family of material point i and V_j represents the volume of material point j. Note that in (7), it is assumed that the domain is discretized into square subdomains and in each subdomain, there is only one particle.

The equation of motion in (7) is dynamic because of the existence of the inertia term. In this study, we are focusing on quasi-static loadings, therefore, the inertia term can be neglected. By following [43], the PD force is linearized. Afterwards, the direct solution method is

utilized to solve the PD equation of motion [44]. According to [38], the equilibrium equation for the quasi-static case can be obtained as a single matrix–vector equation in the total domain β, as:

$$\mathbf{Kd} = \mathbf{b} \tag{8}$$

where $\mathbf{K}, \mathbf{d}$, and $\mathbf{b}$ are the global stiffness matrix, displacement vector, and force vector of all material points, respectively.

Since peridynamics uses integro-differential equations to define the equations of motion, unlike the classical continuum mechanics theory where partial differential equations are utilized, the application of boundary conditions is performed differently. The tractions or point forces cannot be applied as boundary conditions since their volume integrations result in a zero volume [45]. Therefore, the external loads can be applied as body force densities in a real material layer along the boundary of a nonzero volume. The thickness of this layer should be comparable to the size of the horizon [46].

3. Optimization problem statement

A general constrained optimization problem can be expressed as:

$$\min F(\alpha) \tag{9a}$$

$$\textit{subject to}: \begin{cases} X_m(\alpha) = 0 & \text{for } m = 1, 2, \cdots, z \\ Y_n(\alpha) \leq 0 & \text{for } n = 1, 2, \cdots, r \end{cases} \tag{9b}$$

where α is the unknown that we seek to find, $F(\alpha)$ is the objective function, $X_m(\alpha)$ are equality constraints and $Y_n(\alpha)$ are inequality constraints. A multi-material topology optimization problem can be defined as finding the optimum distribution of $p \in \mathbb{N}$ $(p \geqslant 2)$ numbers of distinct materials over a fixed nonempty design domain Ω such that a set of constraint(s) are satisfied. In this work, the objective is to maximize the stiffness of the structure, which is equivalent to minimizing compliance. However, it is worth mentioning that minimizing compliance as a measure of flexibility of the structure in an average manner does not necessarily imply that the maximum displacement at the critical point of the structure is minimized too.

The design variables are set to values in the range of 1 and 0 for each of the materials. The material distribution is determined by the local volume fraction fields, α_k^i $(k = 1, 2, \cdots, p;\ i = 1, 2, \cdots, N)$ for $p - 1$ solid materials, one void phase and N material points. The following upper and lower bounds can be defined for the local volume fractions:

$$l_k \leqslant \alpha_k^i \leqslant u_k,\ \ k = 1, 2, \cdots, p \tag{10}$$

where $0 \leqslant l_k \leqslant u_k \leqslant 1$. Since no overlaps and gaps are allowed in the structure, the summation of all of the local volume fractions for each point $\boldsymbol{x} \in \Omega$ should be equal to one. Therefore:

$$\sum_{k=1}^{p} \alpha_k^i = 1 \tag{11}$$

Moreover:

$$\int_{\Omega} \alpha_k^i d\Omega = \Lambda_k, \quad \sum_{k=1}^{p} \Lambda_k = \Lambda_0 \tag{12}$$

where Λ_k and Λ_0 are the user-defined volume of the kth phase and the volume of the whole design domain, respectively. In other words, $\Lambda_k = \omega_k \Lambda_0$; where ω_k is the local volume constraint on each phase.

In TO problems, the local material properties are local functions of volume fractions of the contributing phases. According to (6), the objective function (the strain energy of the structure) is a function of elastic modulus. Therefore, here, the elastic moduli of material points are considered as the local material properties. In order to compute these properties, the SIMP method is used, which utilizes the power-law interpolation scheme to define the elastic modulus of material point j as a function of design variables (volume fractions). The SIMP interpolation can be expressed as follows:

$$E_i = \sum_{k=1}^{p} \left(\alpha_k^i\right)^q E_k^s \tag{13}$$

where q is the penalization factor, and E_k^s is the elastic modulus corresponding to the kth phase.

The motivation for developing the alternating active phase algorithm is to provide a general framework to convert binary phase topology optimization into multi-phase ones by minimal effort and modification, plus, keeping the robustness and the efficiency of the original algorithms [14]. In this method, the optimization calculations are done through inner loops. In each inner loop, a two-phase topology sub-problem is solved by fixing the topologies of $p - 2$ phases to the last known values, so that those of the two remaining phases (active phases) can vary. If active phases are denoted by 'a' and 'b', then their volume fraction field, r_{ab}, which varies during every binary phase topology optimization sub-problem can be obtained from the following equation:

$$r_{ab}^i = 1 - \sum_{\substack{k=1 \\ k \neq \{a,b\}}}^{p} \alpha_k^i \tag{14}$$

It is only required to take the volume fraction of a as the design variable of the sub-problem because after solving each of them, the volume fraction of phase b (background phase) can be calculated as:

$$\alpha_b^i = r_{ab}^i - \alpha_a^i \tag{15}$$

In each inner loop, the temporary upper bound for phase a can be modified as:

$$u_a^{i,temp} = \min\left(u_a, r_{ab}^i\right) \tag{16}$$

Note that there is no need to modify the lower bound.

Therefore, the internal binary-phase topology optimization solver can be expressed as:

$$\min C\left(\boldsymbol{\alpha}_{ab}^i\right) \tag{17a}$$

$$s.t. \begin{cases} \mathbf{Kd} = \mathbf{b} \\ \int_{\Omega} \alpha_a^i d\Omega = \Lambda_a \\ E_i = \sum_{k=1}^{p} \left(\boldsymbol{\alpha}_{ab}^i\right)^q E_k^s \\ l_a^i \leqslant \alpha_a^i \leqslant u_a^{i,temp} \end{cases} \tag{17b}$$

where $\boldsymbol{\alpha}_{ab}^i = \left\{\alpha_1^i, \alpha_2^i, \cdots, \alpha_p^i\right\}$ is the design vector in which α_a^i and α_b^i could be varied and α_k^i is fixed for $k \neq \{a, b\}$. The volume constraint of the background phase, b, is determined by (14) and (15). Parameter C represents the overall compliance of the structure. Since the value of the total compliance is numerically two times greater than the overall strain energy, we can minimize the strain energy of the structure expressed in (6), instead of compliance. Therefore, in (17a), parameter C can be replaced by parameter U.

Because of the nonlinear nature of the topology optimization problem, the internal optimization solver uses an iterative algorithm. As a result, it needs a convergence criterion. Here, an infinity norm, $||.||_{\infty}$, of changes in the design vector during two consecutive iterations is used as a criterion. That is, when the maximum of local variations in the volume fractions is smaller than a threshold, the iterations are stopped, and the last design vector is reported as an optimal solution. Besides, an upper bound on the number of iterations can be imposed as a stopping criterion.

It is worth mentioning that the active phase algorithm is based on two assumptions. First, the iterations of the internal sub-problem solver are strictly feasible with respect to all the constraints. Second, in

each internal loop, the objective function decreases monotonically as the iterations of the internal algorithm proceed.

According to all the work above, the multi-material topology optimization problem, using active phase algorithm and SIMP method, can be formulated as:

$$\min U = \sum_{i=1}^{N} W(x_i) V_i \tag{18a}$$

$$s.t. \begin{cases} \mathbf{Kd} = \mathbf{b} \\ E_i = \sum_{k=1}^{p} \left(\alpha_k^i\right)^q E_k^s \\ \sum_{k=1}^{p} \omega_k \Lambda_0 = \Lambda_0 \\ 0 \leqslant \omega_k \leqslant 1 \\ 0 \leqslant \alpha_{min} \leqslant \alpha_k^i \leqslant 1 \end{cases} \tag{18b}$$

where the value of α_{min} is set to be a very small but non-zero number to avoid the singularity of the structural stiffness matrix.

Also, the active phase algorithm can be summarized in the flowchart illustrated in Fig. 2.

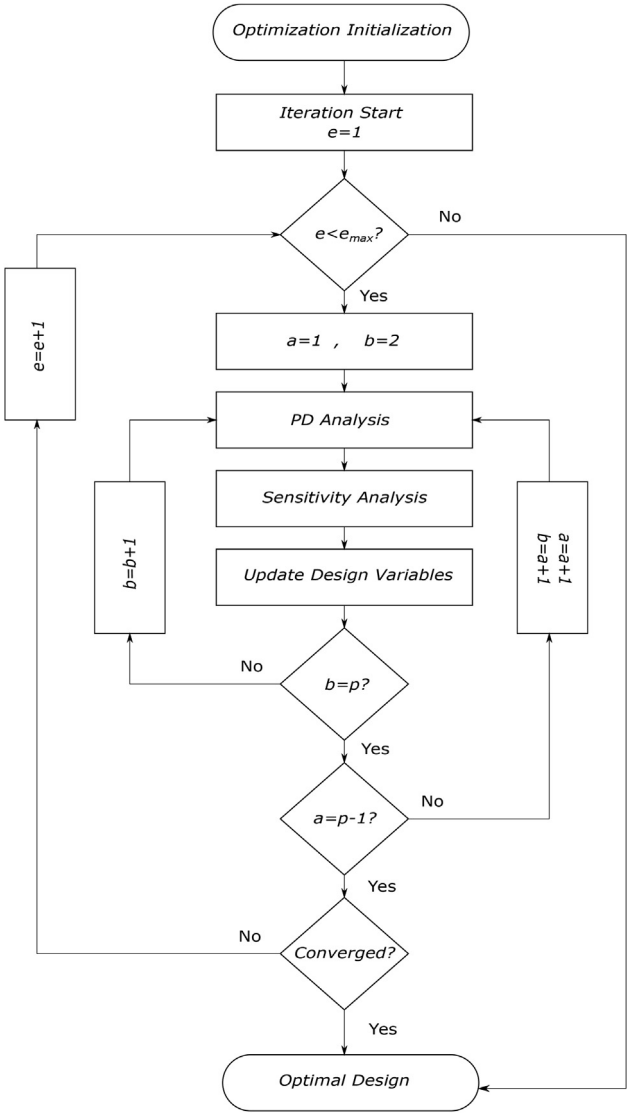

Fig. 2. flowchart of an alternating active-phase algorithm.

3.1. Weighted bonds in PD for topology optimization purposes

During the topology optimization process, some binary-phase regions containing phases with very different material properties (e.g., void and solid) can appear. On the other hand, the value of the bond-constant in (5) is a function of these material properties (here, Young's modulus) and it is obtained by assuming that the material points i and j have the same Young's modulus. Therefore, due to the fact that the contribution of particles i and j is different, it is necessary to consider the influence of their different material properties on the bond connecting them. To do so, a weighting approach proposed in [47] for functionally graded materials is utilized in this study. Young's modulus of the two material points can be defined proportional to the effect of the bond as:

$$E_{ij} = \mu E_i + \kappa E_j \tag{19}$$

where

$$\mu = \frac{E_j}{E_i + E_j}; \quad \kappa = \frac{E_i}{E_i + E_j} \tag{20}$$

By redefining Young's modulus used in (5), the bond-constant value is modified. For instance, if material point i is solid and material point j is void such that $E_j \ll E_i$, the value of E_{ij} in (19) will converge to E_j. Hence, the magnitude of the bond-constant is negligible, resulting into zero interaction and strain energy density. On the other hand, if the two material points are the same, such that $E_i = E_j$, the value of E_{ij} will converge to E_i which does not result in any alteration in the magnitude of the bond-constant between material points i and j.

4. Optimality criteria method

The optimization problem in (18) can be solved using several different methods such as Optimality Criteria (OC), Sequential Linear Programming (SLP), and so forth. Due to its simplicity, the OC approach [48] is used in this study. In this method, a heuristic scheme is utilized to update the design variables as:

$$\alpha_e^{new} = \begin{cases} \max(0, \alpha_e - M) & \text{if} \quad \alpha_e B_e^{\zeta} \leqslant \max(0, \alpha_e - M) \\ \alpha_e B_e^{\zeta} & \text{if} \quad \max(0, \alpha_e - M) \leqslant \alpha_e B_e^{\zeta} \leqslant \min(1, \alpha_e + M) \\ \min(1, \alpha_e + M) & \text{if} \quad \alpha_e B_e^{\zeta} \geqslant \min(1, \alpha_e + M) \end{cases} \tag{21}$$

where M (move) is a positive move-limit which can be chosen by experiment, in order to obtain a suitable, rapid, and stable convergence of the iterations. In (21), $\zeta(= 1/2)$ is a numerical damping coefficient, and B_e is obtained from the optimality condition for the eth iteration as:

$$B_e = \frac{-\frac{\partial U}{\partial \alpha_e}}{\lambda \frac{\partial V}{\partial \alpha_e}} \tag{22}$$

where λ is the Lagrangian multiplier that must be chosen such that the volume constraint is satisfied. Its appropriate value can be found through a bisection algorithm.

The sensitivities of the objective function, U, and the material point volume, V, with respect to the local volume fractions, can be obtained as:

$$\frac{\partial U}{\partial \alpha_e} = -q(\alpha_e)^{q-1} U_e^s \tag{23}$$

$$\frac{\partial V}{\partial \alpha_e} = 1 \tag{24}$$

In (23), U_e^s is the strain energy of solid particles. According to this equation, it can be stated that the sensitivity of void particles with a negligible value for density is equal to zero when the penalization coefficient, q goes to infinity. In (24), it is assumed that each particle has unit volume.

In each inner loop of binary-phase topology optimization, the strain energy of a particle can be stated based on the multiplication of penalized design variable and the strain energy of the solid particle as:

$$U_i = (\alpha_e)^q U_e^s \tag{25}$$

where U_i is the strain energy of each particle. To calculated its value at each optimization iteration, first the solution to the displacement field should be found as:

$$U_i = W(x_i)V_i \tag{26}$$

5. Filtering

Two types of filtering techniques can be used to eliminate the instabilities and checkerboard patterns: application of a filter to either the sensitivities or the densities. In this work, the former method is adopted. For filtering purposes, a circular sub-domain with the radius of R_{min} is defined at the centroid of the ith particle, which includes a set of neighbor particles, n. These adjacent particles influence the sensitivity of the ith particle proportionately to the distance between these two particles, R_{in}. Using the Shepard interpolation scheme, the modified sensitivities at each particle in the OC approach is as follows:

$$\widehat{\frac{\partial U}{\partial \alpha_i}} = \frac{1}{\alpha_i \sum_{n=1}^{N_i} \psi(R_{in})} \sum_{n=1}^{N_i} \alpha_n \psi(R_{in}) \frac{\partial U}{\partial \alpha_n} \tag{27}$$

where $R_{in} = |\boldsymbol{x}_n - \boldsymbol{x}_i|$ is the distance between particles i and n, N_i is the total number of particles in the sub-domain of material point i, and $\psi(R_{in})$ is a weighting function (convolution operator) defined as:

$$\psi(R_{in}) = \begin{cases} R_{min} - R_{in} & \text{if} \quad R_{in} \leqslant R_{min} \\ 0 & \text{if} \quad R_{in} > R_{min} \end{cases} \tag{28}$$

Note that the weighting function decays linearly with the distance from material point n. Therefore, instead of the original sensitivity in (23), the modified sensitivity obtained in (27) is used in the Optimality Criteria update in (22). The filter radius can be interpreted as a design constraint; literature shows that the bigger R_{min} is, the thicker the inner links will become. Also, decreasing the minimum filter radius can rise the number of the inner links [38].

6. Examples and discussion

To investigate the proposed approach, the results of three case studies reported in [24] are compared against our results. These cases investigate the effect of the direction of an interior crack on the optimal topology of a bridge design domain loaded by a concentrated force. Next, four examples are carried to evaluate the robustness of the current method for multi-material TO problems. The impact of an initially embedded crack on the structure is studied in the *cantilever beam*, *L-shape structure* and the *bridge with uniform pressure load* examples. Furthermore, the problem of multi-material topology optimization is solved using three and four phases for a bridge structure. Moreover, the total displacement and strain energy density distributions are provided for all the case-studies in order to investigate the influence of cracks. In order to have a better presentation of the strain energy density distribution, its mean value is taken as the maximum and any values higher than that are depicted as the maximum.

For all of the examples mentioned above, the value of the penalization factor is assumed to be three. According to [49] when the penalization factor is equal or greater than three, the SIMP model obeys Hashin–Shtrikman bounds and the prevailing of some intermediate densities does not exist. To represent different phases, four colours are used: red, blue, green, and white. As the colours change from red to white, the elastic modulus decreases consecutively with red as the hardest and white the softest materials (i.e. void). It should be noted that all the forces are applied to particles as a body force.

6.1. The effect of the direction of interior cracks

In this case study, the impact of the direction of an interior crack on the optimal topology is investigated in three different orientations: an inclined, a horizontal, and a vertical crack with the same length (Fig. 3). The length of the crack and its distance from the right edge are: $l_c = 15.5, t_c = 9.25$, respectively. The length of the structure is $L = 40$ and the height is $H = 20$. Accordingly, the design domain is discretized into 40×20 particles. The left bottom corner is fixed and the right bottom corner is simply supported. The magnitude of the applied force at the middle of the upper edge is $F = 200$. The total volume constraint is chosen to be 40%. Moreover, the volume constraint for the hard material ($E = 400 \times 10^3$) is 15% and for the soft material ($E = 200 \times 10^3$) is 25%. To alleviate singularities in the stiffness matrix, the value of Young's modulus of the void phase is considered to be 10. Also, the value of the minimum filter radius is 1.5.

Fig. 4 displays a comparison between the PD-TO results (left column) with those from [24], where the alternating active-phase algorithm is used with X-FEM (right column). As it can be seen from the PD-TO solutions, the direction of the interior crack can significantly change the optimal topology. Besides, the stiff material (in red) is mostly distributed over the regions with high strain energy for different crack orientations. Comparing the optimal results of these two methods indicates that the structures are generally very similar; however, there are some differences. The final topologies in [24] have multiple intermediate-phase areas where the optimization has not completely converged. This issue can be a result of the insufficient number of elements/design variables. Conversely, in the current method, we could achieve relatively better results in terms of convergence and connectivity of materials by using the same number of design variables. However, the topologies obtained from X-FEM method have slightly lower compliance relative to the PD-TO solutions. This is due to the fact that the compliance values of X-FEM and PD are evaluated based on two different theories. Specifically, Peridynamics is a non-local theory and calculates the strain energy density using non-local interactions of material points whereas X-FEM used in Ref. [24] is a local method and utilizes CCM for its strain energy calculation. On the other hand, the surface correction factors are not considered in PD-TO to reduce the computational cost. Hence, an accurate quantitative comparison of the compliance values of PD-TO and X-FEM can only be considered if the final topologies obtained from PD and X-FEM are both modelled in one of the theories. Additionally, the total displacement and strain energy density distributions obtained from PD analysis are illustrated in Fig. 5.

It is notworthy that the X-FEM method does not provide an easy way to study the emergence and evolution of cracks. Namely, it requires some extra techniques to do so, in particular level-set methods, virtual crack closure, etc. Whereas, PD needs no special techniques to either predict damage initiation/growth in unspecified locations or control multiple damage sites and their complex interactions. Alternatively, it demands only one criterion for all of the above-mentioned processes, which is called the critical failure parameter and is based on energy release rate.

6.2. Example 1: Cantilever Beam

As shown in Fig. 6, a cantilever beam is considered with a concentrated load $F = 1$ at the bottom of its free end. The design domain has a length to height ratio of 3:1. The ratio of Young's modulus for the two solid phases is 2:1. Also, the value of elastic modulus for the void phase is assumed to be 1×10^{-6} to avoid singularities. The volume constraints are 30% and 20% for the hard and soft materials, respec-

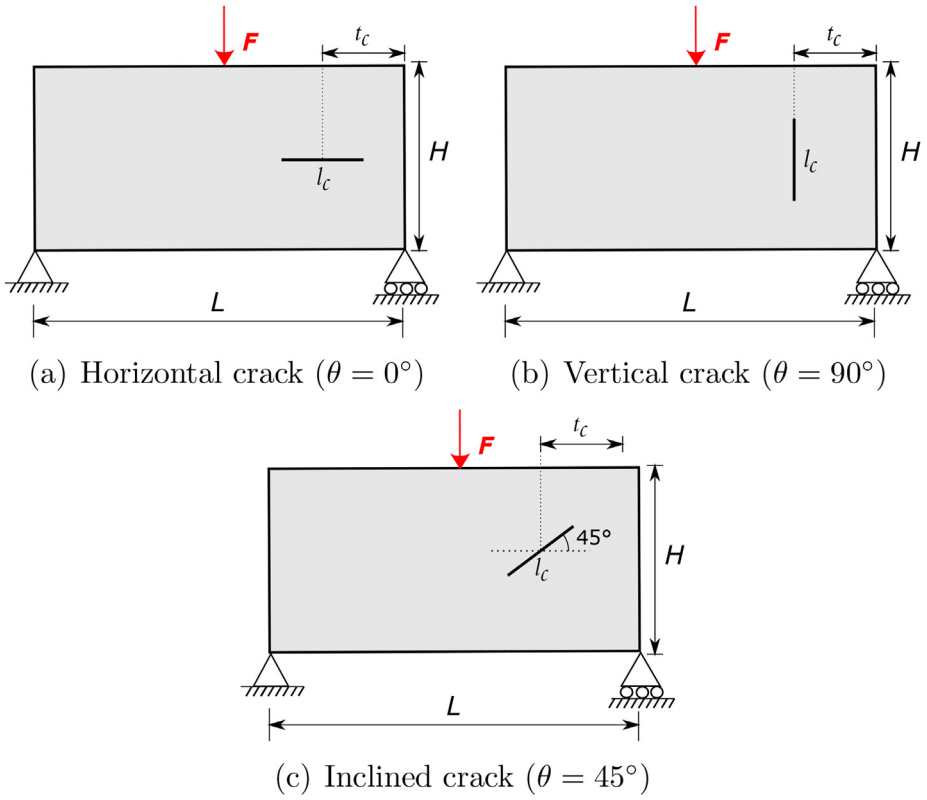

Fig. 3. Studying the effect of the direction of the interior crack.

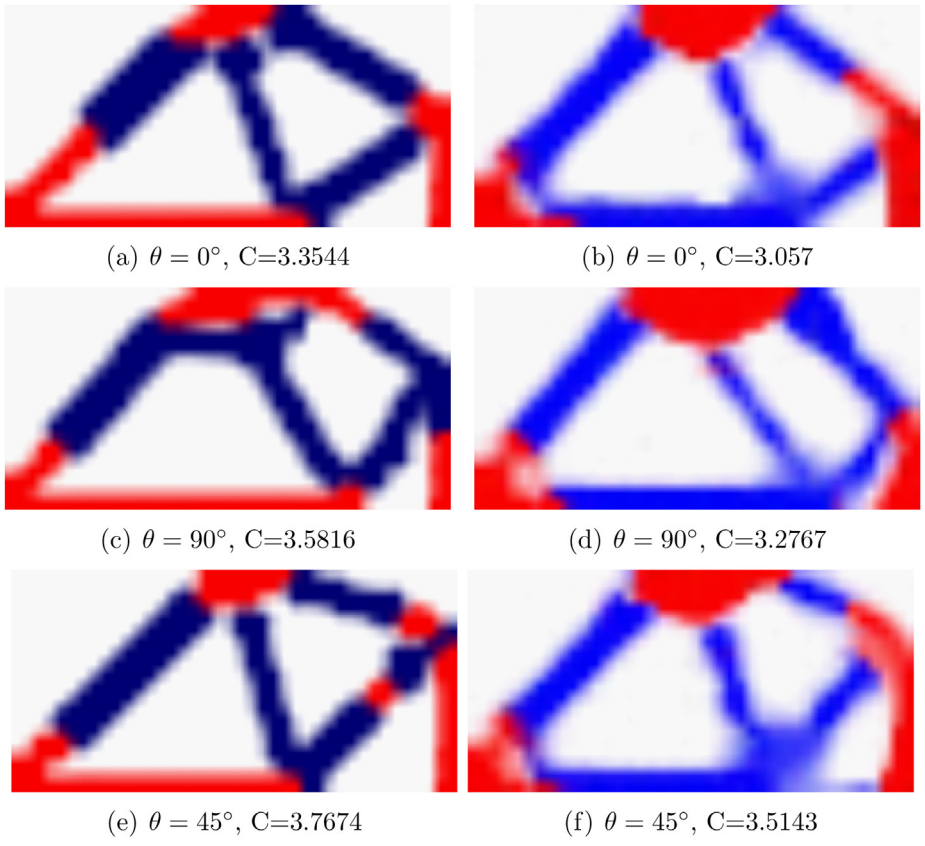

Fig. 4. Comparison of optimal solutions (left column: PD-TO results, right column: X-FEM results).

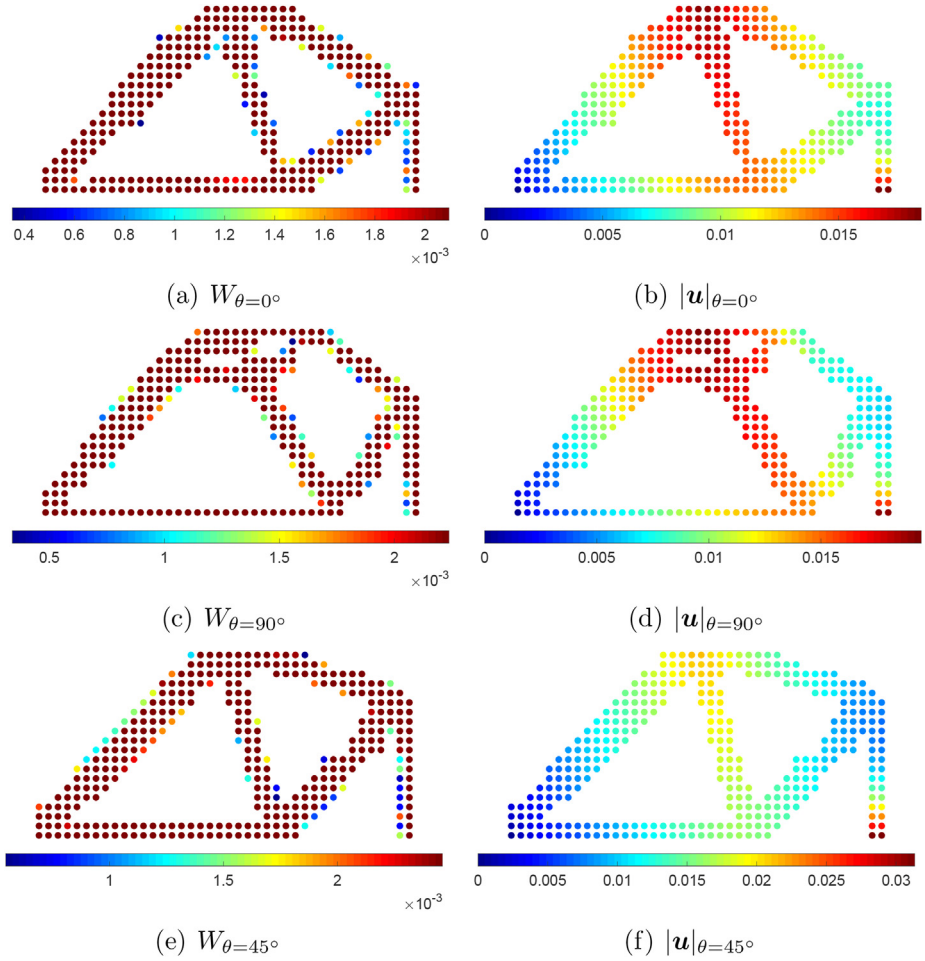

Fig. 5. Strain energy density (left column) and total displacement (right column) distribution of the horizontal, vertical, and inclined interior cracks.

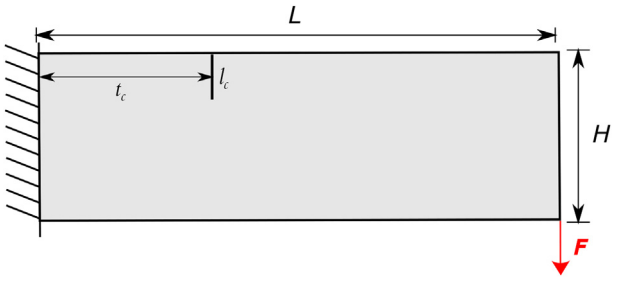

Fig. 6. Design domain of the cantilever beam.

Fig. 7. Optimal design of the cantilever beam with no initial cracks.

Fig. 8. Optimal design of the cantilever beam with an initially embedded crack.

tively, and these solid phases can occupy only 50% of the whole structure. The minimum filter radius is set to be 3. The discretization of the design domain is 90 particles along the length and 30 particles along the height. Also, to study the effect of an embedded crack on the optimal topology, an interior crack is modelled at the upper edge of the beam with the length of $l_c = 0.12H$ and at a distance of $t_c = 0.1166H$ from the fixed end.

Fig. 7 and Fig. 8 display the optimal topologies of the cantilever beam, without and with initial crack, respectively. As can be seen from these figures, adding an initial crack into the structure can significantly affect the final topologies. Also, in the critical regions where the value of the strain energy is typically at its highest value (e.g, where the concentrated force is applied and the area close to the supports) we have the harder material (in red) to minimize the compliance as much as possible. Fig. 9 illustrates the strain energy density and total displacement distributions of the cantilever beam and the effect of the initial crack on them.

6.3. Example 2: L-Shape Structure

Fig. 10 shows the design domain of the L-shape structure and its dimensions with $L = 1$. The beam is fully clamped at the top edge,

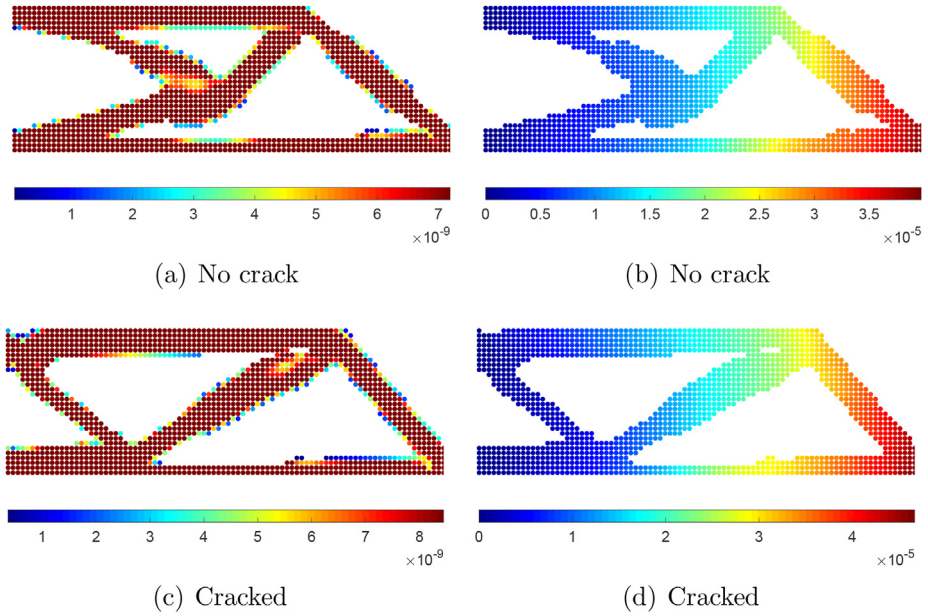

Fig. 9. Strain energy density (left column) and total displacement (right column) distribution of the cantilever beam.

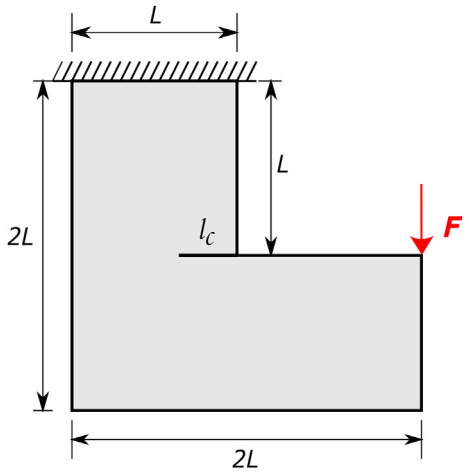

Fig. 10. Design domain of the L-Shape structure.

Fig. 11. Optimal topology of the L-shape beam with no cracks.

and a downward concentrated force is applied to the structure with the magnitude of $F = 30$. The elastic modulus values are assumed to be the same as in Example 1. The corresponding volume constraints are 35% for the hard material, 20% for the soft material, and 45% for the void phase. Also, the minimum filer radius is equal to 3. A square-shape domain (including the L-shape design domain and the void area at the top right) is discretized by 60×60 material points. Moreover, the impact of an interior crack is studied by considering a horizontal crack of the length $l_c = 0.1L$ at the knee.

First, this example is solved without considering the crack, and the result is shown in Fig. 11. Similar to the previous case, the critical areas close to the support and the location the concentrated force is applied are filled with the hard material to increase the stiffness of the structure. Next, the same example is solved, this time by taking into account an initial crack at the knee. Fig. 12 illustrates that the distribution of the hard material (red color) has changed close to the crack tips to prevent crack propagation. Furthermore, Fig. 13 portrays the distribution of the strain energy density and total displacement of the L-Shape structure without and with initially embedded cracks.

Fig. 12. Optimal topology of the L-shape beam with an embedded crack at the knee.

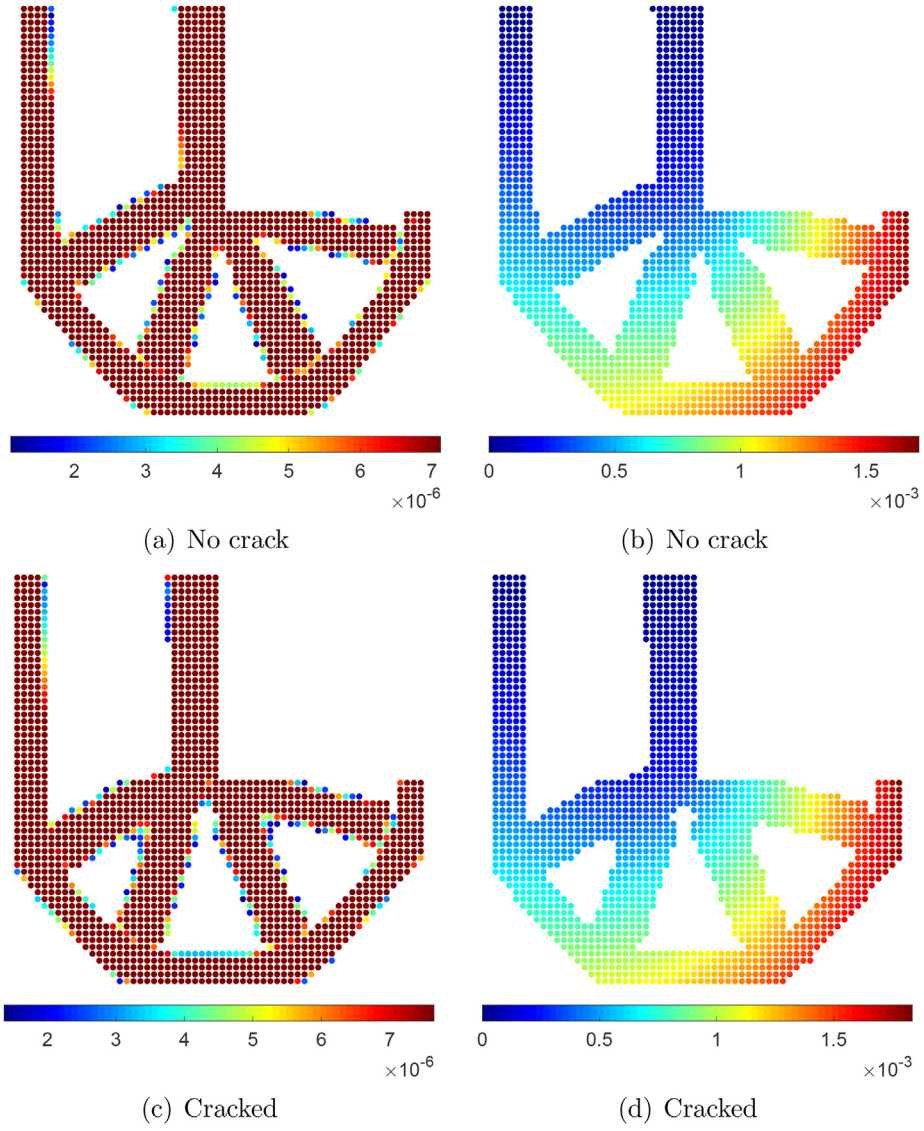

Fig. 13. Strain energy density (left column) and total displacement (right column) distribution of the L-Shape structure.

6.4. Example 3: Bridge with Uniform Pressure Load

In this example, a bridge, fully fixed at left and right edges is loaded by a uniform pressure $P = 1$. The length of the structure is two times greater than its width, and there are 80 and 40 particles along the length and the width of the bridge, respectively (Fig. 14). The elastic

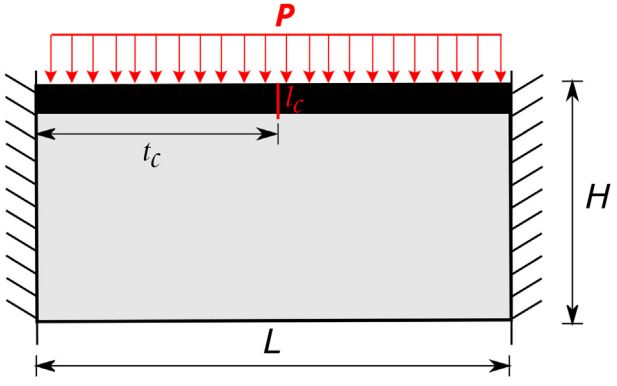

Fig. 14. Design domain of the bridge with uniform pressure load.

Fig. 15. Optimal topology of the bridge under uniform pressure without initial crack.

Fig. 16. Optimal topology of the bridge under uniform pressure with an initially embedded crack.

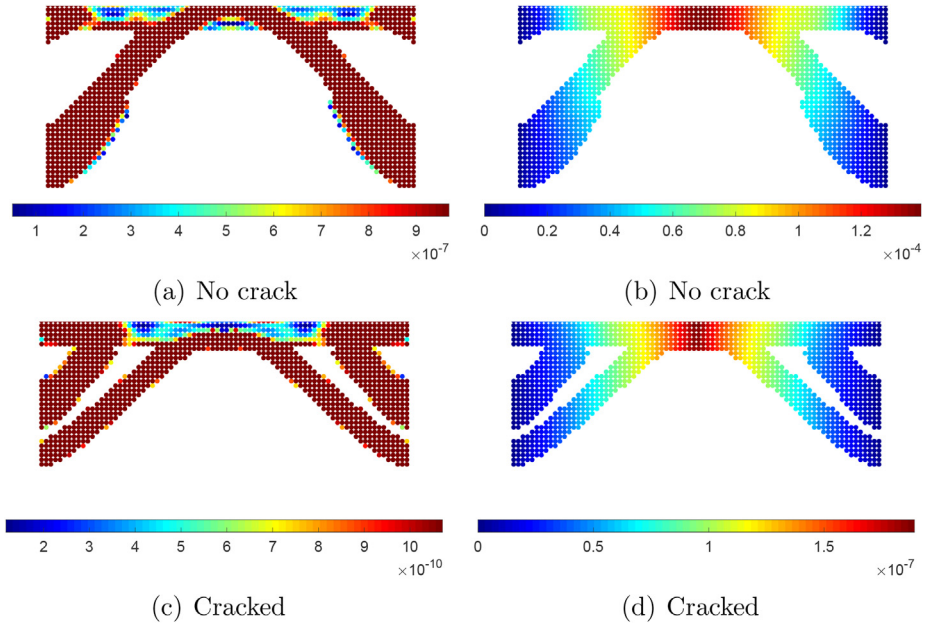

Fig. 17. Strain energy density (left column) and total displacement (right column) distribution of the bridge under uniform pressure.

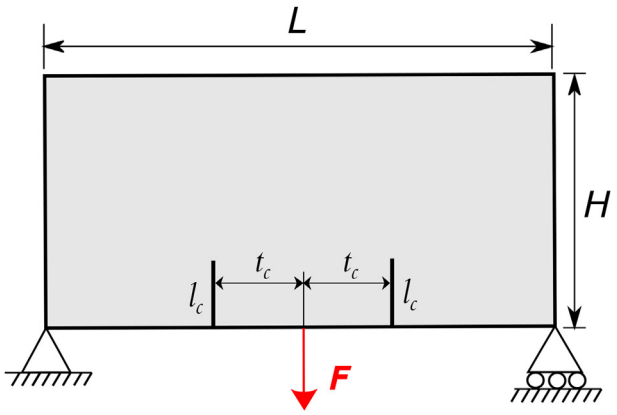

Fig. 18. Design domain of the bridge with two interior cracks.

modulus ratio of the hard to the soft material is 2:1. The value of Young's modulus of the void phase is the same as the previous cases. The volume constraints of hard and soft materials are 30% and 10%, respectively. The value of the minimum filter radius is assumed to be 3. A fixed layer of 6 particles in the vertical direction is considered; that is, the material points located in this area are fixed to have the hard material's Young's modulus, and it does not change throughout the optimization process. In addition, a crack of the length $l_c = 0.11H$ and at $t_c = 0.5L$ is modeled at the upper edge that passes through the fixed layer.

Fig. 19. Optimal result of the three-material bridge structure.

Fig. 20. Optimal result of the four-material bridge structure.

The optimal topologies of the bridge under uniform pressure are illustrated in Fig. 15 for the structure without a crack and in Fig. 16 for the cracked structure. By comparing these two figures, it can be stated that when there is an embedded crack, the value of the strain energy increases near the crack tips. Therefore, some extra amount

Table 1
Material properties of each material.

	Number of materials	
Material properties	Three (red, blue, white)	Four (red, blue, green, white)
Young's modulus	$E_r = 2, E_b = 1, E_w = 1 \times 10^{-9}$	$E_r = 2, E_b = 1, E_g = 0.1, E_w = 1 \times 10^{-9}$
Volume fraction	$\omega_r = 35\%, \omega_b = 25\%, \omega_w = 40\%$	$\omega_r = 25\%, \omega_b = 20\%, \omega_g = 15\%, \omega_w = 40\%$

Fig. 21. Optimal result of the three-material cracked bridge structure.

Fig. 22. Optimal result of the four-material cracked bridge structure.

of hard material is added to that region to reduce the magnitude of the strain energy (The small bump at the upper edge in Fig. 16). Moreover, Fig. 17 shows the strain energy density and total displacement distributions and the initial crack's affect on them.

6.5. Example 4: Bridge

The effect of the number of phases on the optimal topology is studied in this example. Fig. 18 shows the design domain of a bridge. A concentrated load $F = 1$ is applied at the middle of the bottom edge. The left bottom corner is fixed, and the right bottom corner is simply supported. Moreover, two vertical cracks are placed at the bottom edge of the bridge at a horizontal distance of $t_c = 0.1L$ from the point where the force is applied. The length of the cracks is $l_c = 0.11H$. The ratio of the length to the height of the structure and the minimum filter radius value are the same as Example 3. The values of the elastic moduli and the volume constraints of the three-phase and four-phase cases are summarized in Table 1. To decrease the computational cost, the symmetry of the structure and the applied loads is taken into account. Therefore, the design domain is discretized into 96×96 particles, distributed evenly over the domain and the target total volume constraint is chosen to be 60%.

The optimal solutions to the bridge problem with no cracks are shown in Fig. 19 and Fig. 20 for three and four material cases, respectively. It can be seen that the topologies are different, which implies the effect of the number of materials on the final topology. Furthermore, the cracked bridge case is solved to study the influence of cracks. Fig. 21 illustrates the final topology of the cracked bridge using two solid materials. The result shows that the lower link in Fig. 19 is removed so that the cracks are located in the void area. Consequently, the algorithm has prevented a rise in the strain energy of the structure. The solution of the cracked bridge using three solid materials is displayed in Fig. 22. The same feature can be seen in this topology where the lower link is deleted compared to Fig. 20. Moreover, Fig. 23 and Fig. 24 demonstrate the distribution of the strain energy and total displacement over the three and four material structures, respectively.

7. Conclusion

The alternating active-phase algorithm is combined with the Peridynamics theory to solve density-based multi-material topology optimization problems. In this work, the direct solution method is used to solve the PD equations. As such, the computational cost of the proposed method is of the same order as mesh-based TO approaches.

First, the validity of the proposed method is investigated by comparing the results of three different cases against a work done by [24], where the same alternating active phase algorithm was used with the X-FEM approach. The results show good compatibility with their topologies while achieving relatively higher convergence. Note that mesh-based methods cannot handle crack modelling in a straightforward manner, and require complex algorithms to do so. Conversely, Peridynamics does not need any special treatments to solve problems involving moving boundary problems, large deformations, and damage presence since there is no necessity to maintain mesh connectivity. Next, the robustness of this method was studied through four examples by taking into account the impact of initial cracks on the optimal topologies.

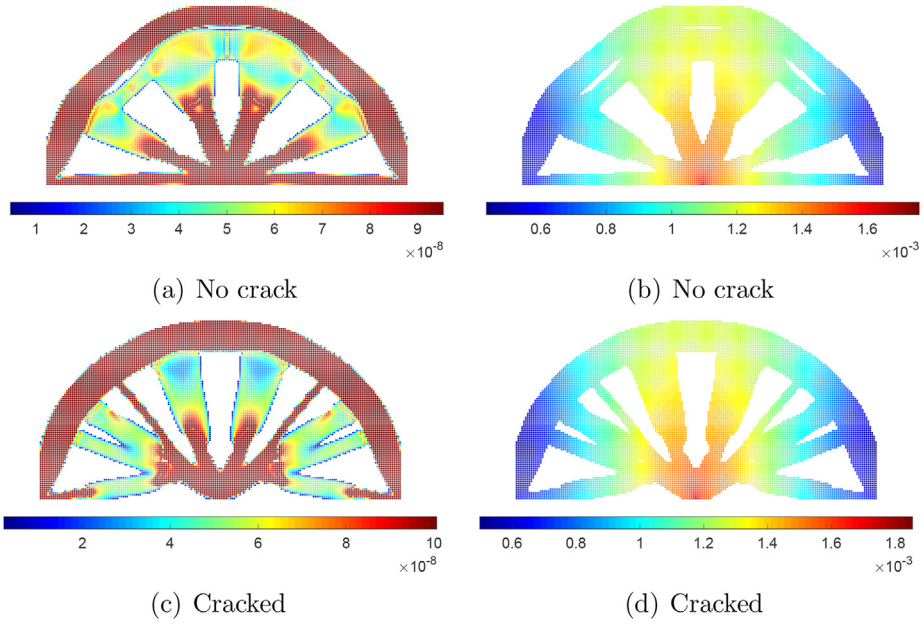

Fig. 23. Strain energy density (left column) and total displacement (right column) distribution of the three-material bridge.

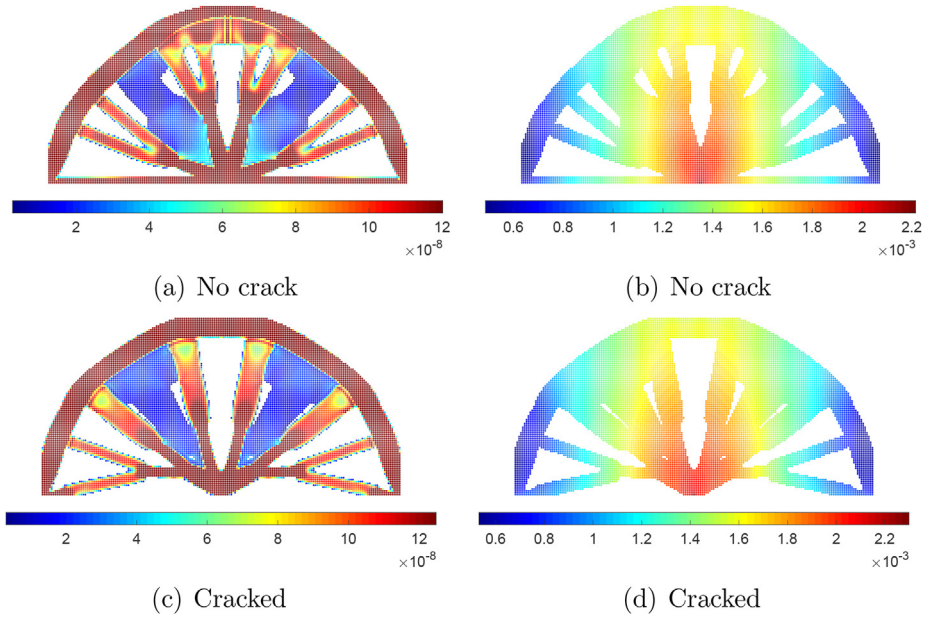

Fig. 24. Strain energy density (left column) and total displacement (right column) distribution of the four-material bridge.

The results show that initial cracks can notably influence the final design of the multi-material structures. In general, the PD-based topology optimization method adds/removes material points such that damaged regions are preferentially populated with material points to hinder crack propagation during/after optimization.

CRediT authorship contribution statement

Anahita Habibian: Methodology, Software, Validation, Formal analysis, Writing - original draft. **Abdolrasoul Sohouli:** Methodology, Software, Validation, Formal analysis, Writing - original draft. **Adnan Kefal:** Methodology, Software, Validation, Formal analysis, Writing - review & editing. **Ben Nadler:** Supervision, Writing - review & editing. **Mehmet Yildiz:** Conceptualization, Resources, Writing - review & editing, Funding acquisition. **Afzal Suleman:** Supervision, Conceptualization, Resources, Writing - review & editing, Funding acquisition.

Declaration of Competing Interest

The authors declare that they have no known competing financial interests or personal relationships that could have appeared to influence the work reported in this paper.

Acknowledgement

A. Suleman acknowledges the research funding by the NSERC Canada Research Chairs Program.

References

[1] Bendsøe MP, Kikuchi N. Generating optimal topologies in structural design using a homogenization method. Comput Methods Appl Mech Eng 1988;71(2):197–224. https://doi.org/10.1016/0045-7825(88)90086-2.
[2] Bendsøe MP. Optimal shape design as a material distribution problem. Struct Optim 1989;1(4):193–202. https://doi.org/10.1007/BF01650949.
[3] Zhou M, Rozvany GI. The COC algorithm, Part II: Topological, geometrical and generalized shape optimization. Comput Methods Appl Mech Eng 1991;89 (1–3):309–36. https://doi.org/10.1016/0045-7825(91)90046-9.
[4] Yin L, Ananthasuresh GK. Topology optimization of compliant mechanisms with multiple materials using a peak function material interpolation scheme. Struct Multidisciplinary Optim 2001;23(1):49–62. https://doi.org/10.1007/s00158-001-0165-z.
[5] Zuo W, Saitou K. Multi-material topology optimization using ordered SIMP interpolation. Struct Multidisciplinary Optim 2017;55(2):477–91. https://doi.org/10.1007/s00158-016-1513-3.
[6] Xie YM, Steven GP. A simple evolutionary procedure for structural optimization. Computers Struct 1993;49(5):885–96. https://doi.org/10.1016/0045-7949(93)90035-C.
[7] Querin OM, Young V, Steven GP, Xie YM. Computational efficiency and validation of bi-directional evolutionary structural optimization. Comput Methods Appl Mech Eng 2000;189(2):559–73. https://doi.org/10.1016/S0045-7825(99)00309-6.
[8] Osher S, Sethian JA. Fronts propagating with curvature-dependent speed: Algorithms based on Hamilton-Jacobi formulations. J Comput Phys 1988;79 (1):12–49. https://doi.org/10.1016/0021-9991(88)90002-2.
[9] Sethian JA, Wiegmann A. Structural Boundary Design via Level Set and Immersed Interface Methods. J Comput Phys 2000;163(2):489–528. https://doi.org/10.1006/jcph.2000.6581.
[10] Xia Q, Wang MY. Simultaneous optimization of the material properties and the topology of functionally graded structures. CAD Computer Aided Design 2008;40 (6):660–75. https://doi.org/10.1016/j.cad.2008.01.014.
[11] Wang MY, Wang X. Color level sets: A multi-phase method for structural topology optimization with multiple materials. Comput Methods Appl Mech Eng 2004;193 (6–8):469–96. https://doi.org/10.1016/j.cma.2003.10.008.
[12] Vese LA, Chan TF. A multiphase level set framework for image segmentation using the Mumford and Shah model. Int J Comput Vision 2002;50(3):271–93. https://doi.org/10.1023/A:1020874308076.
[13] Wang Y, Luo Z, Kang Z, Zhang N. A multi-material level set-based topology and shape optimization method. Comput Methods Appl Mech Eng 2015;283:1570–86. https://doi.org/10.1016/j.cma.2014.11.002.
[14] Tavakoli R, Mohseni SM. Alternating active-phase algorithm for multimaterial topology optimization problems: A 115-line MATLAB implementation. Struct Multidisciplinary Optim 2014;49(4):621–42. https://doi.org/10.1007/s00158-013-0999-1.
[15] Majdi B, Reza A, Multi-material topology optimization of compliant mechanisms via solid isotropic material with penalization approach and alternating active phase algorithm, Proc Inst Mech Eng, Part C: J Mech Eng Sci (2020) 095440622090862 doi:10.1177/0954406220908627. URL http://journals.sagepub.com/doi/10.1177/0954406220908627.
[16] Monaghan J. Smoothed particle hydrodynamics and its diverse applications. Annu Rev Fluid Mech 2012;44(1):323–46. https://doi.org/10.1146/annurev-fluid-120710-101220.
[17] Belytschko T, Lu YY, Gu L. Element-free Galerkin methods. Int J Numer Meth Eng 1994;37(2):229–56. https://doi.org/10.1002/nme.1620370205.
[18] Atluri SN, Zhu T. A new Meshless Local Petrov-Galerkin (MLPG) approach in computational mechanics. Comput Mech 1998;22(2):117–27. https://doi.org/10.1007/s004660050346.
[19] Liu WK, Jun S, Zhang YF. Reproducing kernel particle methods. Int J Numer Meth Fluids 1995;20(8–9):1081–106. https://doi.org/10.1002/fld.1650200824.
[20] Luo Z, Zhang N, Gao W, Ma H. Structural shape and topology optimization using a meshless Galerkin level set method. Int J Numer Meth Eng 2012;90(3):369–89. https://doi.org/10.1002/nme.3325.
[21] Cui M, Chen H, Zhou J, Wang F. A meshless method for multi-material topology optimization based on the alternating active-phase algorithm. Eng Computers 2017;33(4):871–84. https://doi.org/10.1007/s00366-017-0503-4.

[22] Zhang Y, Ge W, Zhang Y, Zhao Z. Topology optimization method with direct coupled finite element–element-free Galerkin method. Adv Eng Softw 2018;115:217–29. https://doi.org/10.1016/j.advengsoft.2017.09.012.
[23] Shobeiri V. The topology optimization design for cracked structures. Eng Anal Boundary Elem 2015;58:26–38. https://doi.org/10.1016/j.enganabound.2015.03.002.
[24] Banh TT, Lee D. Multi-material topology optimization design for continuum structures with crack patterns. Compos Struct 2018;186:193–209. https://doi.org/10.1016/j.compstruct.2017.11.088.
[25] Silling SA. Reformulation of elasticity theory for discontinuities and long-range forces. J Mech Phys Solids 2000;48(1):175–209. https://doi.org/10.1016/S0022-5096(99)00029-0.
[26] Silling SA, Epton M, Weckner O, Xu J, Askari E. Peridynamic states and constitutive modeling. J Elast 2007;88(2):151–84. https://doi.org/10.1007/s10659-007-9125-1.
[27] Silling SA, Askari E, A meshfree method based on the peridynamic model of solid mechanics. In: Computers and Structures, Vol. 83, Pergamon, 2005, pp. 1526–1535. doi:10.1016/j.compstruc.2004.11.026..
[28] Basoglu MF, Zerin Z, Kefal A, Oterkus E. A computational model of peridynamic theory for deflecting behavior of crack propagation with micro-cracks. Comput Mater Sci 2019;162:33–46. https://doi.org/10.1016/j.commatsci.2019.02.032.
[29] Hu W, Ha YD, Bobaru F. Peridynamic model for dynamic fracture in unidirectional fiber-reinforced composites. Comput Methods Appl Mech Eng 2012;217–220:247–61. https://doi.org/10.1016/j.cma.2012.01.016.
[30] AlKhateab B, Tabrizi IE, Zanjani JSM, Rahimi MN, Poudeh LH, Kefal A, Yildiz M. Damage mechanisms in CFRP/HNT laminates under flexural and in-plane shear loadings using experimental and numerical methods. Compos Part A: Appl Sci Manuf 2020;136. https://doi.org/10.1016/j.compositesa.2020.105962. 105962.
[31] Jung J, Seok J. Fatigue crack growth analysis in layered heterogeneous material systems using peridynamic approach. Compos Struct 2016;152:403–7. https://doi.org/10.1016/j.compstruct.2016.05.077.
[32] Silling SA. Dynamic fracture modeling with a meshfree peridynamic code. In: Computational Fluid and Solid Mechanics 2003. Elsevier Inc.; 2003. p. 641–4. https://doi.org/10.1016/B978-008044046-0.50157-3.
[33] Huang D, Lu G, Liu Y. Nonlocal peridynamic modeling and simulation on crack propagation in concrete structures. Math Problems Eng 2015;2015. https://doi.org/10.1155/2015/858723.
[34] le Hu Y, Yu Y, Wang H. Peridynamic analytical method for progressive damage in notched composite laminates. Compos Struct 2014;108(1):801–10. https://doi.org/10.1016/j.compstruct.2013.10.018.
[35] Cheng Z, Zhang G, Wang Y, Bobaru F. A peridynamic model for dynamic fracture in functionally graded materials. Compos Struct 2015;133:529–46. https://doi.org/10.1016/j.compstruct.2015.07.047.
[36] Ozdemir M, Kefal A, Imachi M, Tanaka S, Oterkus E. Dynamic fracture analysis of functionally graded materials using ordinary state-based peridynamics. Compos Struct 2020;244:. https://doi.org/10.1016/j.compstruct.2020.112296112296.
[37] Hu YL, Madenci E. Peridynamics for fatigue life and residual strength prediction of composite laminates. Compos Struct 2017;160:169–84. https://doi.org/10.1016/j.compstruct.2016.10.010.
[38] Kefal A, Sohouli A, Oterkus E, Yildiz M, Suleman A. Topology optimization of cracked structures using peridynamics. Continuum Mech Thermodyn 2019;31(6):1645–72. https://doi.org/10.1007/s00161-019-00830-x.
[39] Sohouli A, Kefal A, Abdelhamid A, Yildiz M, Suleman A. Continuous density-based topology optimization of cracked structures using peridynamics. J Struct Multidisciplinary Optim 2020. https://doi.org/10.1007/s00158-020-02608-1.
[40] Gao T, Zhang W. A mass constraint formulation for structural topology optimization with multiphase materials. Int J Numer Meth Eng 2011;88(8):774–96. https://doi.org/10.1002/nme.3197.
[41] Gao T, Xu P, Zhang W. Topology optimization of thermo-elastic structures with multiple materials under mass constraint. Computers Struct 2016;173:150–60. https://doi.org/10.1016/j.compstruc.2016.06.002.
[42] Yang X, Li M. Discrete multi-material topology optimization under total mass constraint. CAD Computer Aided Design 2018;102:182–92. https://doi.org/10.1016/j.cad.2018.04.023.
[43] Silling SA. Linearized theory of peridynamic states. J Elast 2010;99(1):85–111. https://doi.org/10.1007/s10659-009-9234-0.
[44] Bobaru F, Yang M, Alves LF, Silling SA, Askari E, Xu J. Convergence, adaptive refinement, and scaling in 1D peridynamics. Int J Numer Meth Eng 2009;77(6):852–77. https://doi.org/10.1002/nme.2439.
[45] Madenci E, Oterkus E, Peridynamic theory and its applications, Vol. 9781461484, Springer, New York, 2014. doi:10.1007/978-1-4614-8465-3..
[46] Macek RW, Silling SA. Peridynamics via finite element analysis. Finite Elem Anal Des 2007;43(15):1169–78. https://doi.org/10.1016/j.finel.2007.08.012.
[47] Cheng ZQ, Sui ZB, Yin H, Yuan CF, Chu LS. Studies of dynamic fracture in functionally graded materials using peridynamic modeling with composite weighted bond. Theoret Appl Fract Mech 2019;103:. https://doi.org/10.1016/j.tafmec.2019.102242102242.
[48] Bendsøe MP, Bendsøe MP. Introduction. In: Optimization of Structural Topology, Shape, and Material. Berlin Heidelberg: Springer; 1995. p. 1–4. https://doi.org/10.1007/978-3-662-03115-5_1.
[49] Bendsøe MP, Sigmund O. Material interpolation schemes in topology optimization. Arch Appl Mech 1999;69(9–10):635–54. https://doi.org/10.1007/s004190050248.